Cerebral haemodynamics at varying oxygen saturation levels in the near-infrared optical transparency window

Abstract. Novel biomedical technologies based on light interaction with biological tissues can pave the way towards inexpensive, non-invasive diagnostics with constant monitoring capabilities. Current diagnostics techniques utilise such features, but unfortunately not all of them simultaneously. As medical imaging modalities, they can produce images with high molecular sensitivity and high spatial resolution, which is not currently achieved by imaging technologies such MRI and CT. This project focuses on utilising near-infrared light for the detection of changes in the oxy-deoxy haemoglobin concentration in the brain with decreasing oxygen saturation levels through quantification of light transport. A five-layered tetrahedral mesh-based model of the adult head was constructed from a head atlas using open-source software. Monte Carlo simulations were used to obtain the fluence distribution inside the model at different oxygen saturation levels at four different wavelengths of light. The results clearly show that singular assessment at 650 nm and 700 nm wavelengths, the decrease in the amount of fluence is noticeable as the cerebral oxygen saturation decreases, even at small such changes. However, for the 900 nm and 1100 nm, the fluence decrease is not prominent enough to conclude any utility of those wavelengths for the scope of the project. An elaborate discussion is presented regarding the applications of the experiment such as modelling the cerebral haemodynamic response for detection of abnormal functioning of a specific brain region or even for brain atrophy. The limitations of the project and further work are detailed, along with possible computational and anatomical improvements of the model.

1. Introduction

Biomedical optics is a promising candidate for the development of medical equipment for non-invasive diagnostics and therapeutics applications. A multidisciplinary field that involves the study of light with biological tissues with the scope of developing novel technologies for use in clinical applications and healthcare, has already produced optical bioimaging technologies that exhibit high spatial resolution and high molecular sensitivity with decreased costs of operation [1]. Optical Coherence Tomography (OCT) used for real-time 3D imaging, and Diffuse Optical Imaging (DOI), used to image blood oxygenation in vivo are two such techniques that extend the capabilities of optics into the medical diagnostics sector [2,3]. Compared to established imaging modalities such as MRI and CT, biomedical technologies utilising light provide increased safety due to the non-radioactive nature of light and the non-invasiveness of the clinical procedure; along with the capability of constant patient monitoring at the region of clinical interest [1,4,5]. The major drawback, however, with optical technologies is that light does not penetrate deep in tissues due to the large amount of scattering caused by the interacting tissues.

Although the high scattering poses limitations to the depth of light penetration, it also provides a substantial benefit: the absorption of biological tissues is considerably smaller. This is not observed in regions of infrared and ultraviolet, where absorption largely overweighs scattering. At the shorter wavelengths, haemoglobin's absorption largely dominates; at longer wavelengths, a similar absorption

domination is observed by water in the tissues. Current research, therefore, concentrates on the near-infrared region (NIR), with interest on four specific optical transparency windows: NIR-I at 700-1000 nm, NIR-II at 1000-1350 nm, NIR-III at 1550-1870 nm and NIR-IV at 2100-2300 nm [1]. Utilisation of the optical transparency windows is exhibited in near-infrared spectroscopy (NIRS), a non-invasive technique that quantifies the cerebral oxygenation and cerebral haemodynamic responses (assessment of blood perfusion) by measuring the relative changes in the oxygenated and deoxygenated haemoglobin concentrations [6,7]. Studies have shown the effectiveness of NIRS measurements for the effects of physiological events on blood perfusion such as microgravity, orthostatic stress, and aging [8].

This project studies the cerebral haemodynamics, with the objective to assess and quantitively define the effect of oxygen saturation levels in the adult head. A five-layered model of the adult head was created by converting a head atlas from a Neurodevelopmental MRI Database to a tetrahedral mesh for Monte Carlo simulations [9,10]. The NIR-I and NIR-II optical windows were considered, because they are most employed in non-invasive optical bioimaging and tissue behaviour is well characterised in literature for those wavelengths. The corresponding optical properties for each of the tissues considered in the mesh model were obtained from literature by correctly analysing the methodologies used by the authors on obtaining said optical properties, a necessary task due to the broad range of results published in prior literature. The results successfully quantify the difference in oxygen saturation levels, which provides the possibility for the development of a non-invasive medical diagnostics modality for assessment of brain functioning and detection of abnormalities, especially for patients having incurred damage on a specific brain region. There is still a long way ahead into translating such a utility to a medical modality, but the article also addresses improvements and further steps, and distinguishes the multi-effectiveness of such an observation in quantifying other brain-related disorders.

Although it is of undoubtful insight for clinical examinations such as echocardiography, this paper will not analyse the physical principles of brain haemodynamics; for such a detailed analysis, the interested reader can consult the paper from Secomb [11]. Our paper considers the clinical investigation of brain haemodynamics rather than the theoretical examination of the matter, and through simulation-based methodologies, shows that light can be used to detect drops in the cerebral oxygen saturation levels.

2. Theory and Background
The article draws upon current knowledge of optics, Monte Carlo simulations, light transport models and the physiology of the adult head. Therefore, this section is devoted into the introduction of the relevant theories required for the investigation of cerebral haemodynamics by utility of near-infrared wavelengths.

2.1. Light Interaction in Biological Tissue
Light transport phenomena produced by turbid complex media, such as biological tissue, are strongly affected by scattering. Blood, skin, brain and bone are all composed of cellular and subcellular organelles that act as scatterers of light, therefore complicating the light transport processes further. In defining however, a useful and applicable model for predicting the behaviour of light in turbid complex media, relevant assumptions on the properties of light are introduced, along with the determination of tissue optical properties [12].

2.1.1. *Properties of light and light upon an interface.* Interaction of light with matter and the exchange of energy and momentum therein, is best described through the quantum concept of light, in terms of photons. The favourable use of the classical description of light is included where necessary. In the current theory, referred to as the Radiative Transport Theory, the phase, polarisation, and interference properties of light are ignored [12].

The necessity of the classical picture is best viewed at the air-matter and matter-matter interfaces. The refractive index mismatch between the two media gives rise to reflection and transmission of the incident light, hence the need for the use of Fresnel equations, as with the case of transparent materials.

Incident light is approximated as a plane wave and the boundary as being infinitely long compared to the width of the incident beam. The reflected and transmitted intensity are therefore given by [13]:

$$R = \frac{sin^2(\theta_i - \theta_t)}{sin^2(\theta_i + \theta_t)} \qquad (1a)$$

$$T = 1 - R = \frac{4sin\theta_i * sin\theta_t * cos\theta_i * cos\theta_t}{sin^2(\theta_i + \theta_t)} \qquad (1b)$$

R and T are the transmitted and reflected intensities respectively, and θ_i, θ_t are the angles of incidence and transmission. Transmittance and Reflectance are indeed physical quantities that are required in the measurements of the conducted experiment. It is important to mention however, that the Fresnel equations are just an approximation to the transmitted and reflected intensity. This originates from the properties of biological tissues being turbid, geometrically complex (they have uneven, non-smooth surfaces) with spatial variations, and containing scatterers on the boundaries, therefore refractive index mismatch in those occasions differs from region to region for the same tissue.

2.1.2. *The Radiative Transport Theory.* Due to the multiple scattering effects observed in the propagation of light through biological tissue, the Electromagnetic theory renders itself too complicated to be used as an analytical approach. A simplified model, that only considers the transport of light energy in the medium, is used instead. The Radiative Transport theory, which ignores wave phenomena of light and considers the scattered fields to be completely incoherent and largely diffused, has been established empirically as a valid theory for strong scattering optical media. As it is suggestive of the name, the RTT tracks only the transport of light energy inside the medium by considering the spatially averaged energy. The Electromagnetic field is hence replaced with the specific intensity $I(r,\hat{s},t)$ and the medium is defined through three parameters: the absorption coefficient μ_a, the scattering coefficient μ_s, and the scattering phase function $p(\hat{s} . \hat{s}')$ [12].

Scattering inside the tissue is described by the Rayleigh limit, for scatterers much smaller in size than the wavelength of the incident wave, and the Mie limit for scatterers of comparable size to said wavelength. In general, scattering is quantified using the scattering cross-section. The same approach holds valid for a localised absorber, using the absorption cross-section [12].

$$\sigma_s(\hat{s}) = \frac{P_{scatt}}{I_0} \qquad (2a)$$

$$\sigma_a = \frac{P_{abs}}{I_0} \qquad (2b)$$

P_{scatt} and P_{abs} are the amounts of power spatially redirected and absorbed respectively, I_0 is the initial intensity of the incident wave, $\sigma_s(\hat{s})$ and σ_a are the scattering and absorption cross sections. The RTT also holds a rough, but adequate approximation of the scatterers being spherically symmetric; in that regard $\sigma_s(\hat{s}) \rightarrow \sigma_s$. Therefore, for a medium containing a uniform distribution of absorbers and scatterers, the absorption and scattering coefficient are hence represented with:

$$\mu_a = \rho_a \sigma_a \qquad (3a)$$

$$\mu_s = \rho_s \sigma_s \qquad (3b)$$

where ρ_s and ρ_a are the number densities of the scatterers and absorbers, respectively [12].

Setting the approximations and parameters as the preliminaries to the RTT and defining the scattering phase function (SPF) as

$$p(\hat{s} \cdot \hat{s}') = \frac{4\pi}{\sigma_s + \sigma_a} * \frac{d\sigma_s}{d\Omega}(\hat{s} \cdot \hat{s}') \tag{4}$$

we obtain the RT equation, written as the following integrodifferential:

$$\frac{1}{c_m} \frac{\partial I(r, \hat{s}, t)}{\partial t} = -\hat{s} \cdot \boldsymbol{\nabla} I(r, \hat{s}, t) - (\mu_a + \mu_s) I(r, \hat{s}, t)$$

$$+ \frac{(\mu_a + \mu_s)}{4\pi} \int_{4\pi} p(\hat{s} \cdot \hat{s}) I(r, \hat{s}, t) d\Omega' + Q(r, \hat{s}, t) \tag{5}$$

The differential term in equation (4) is the differential cross section describing the angular distribution of the scattered radiation. In equation (5), c_m is the speed of light in the medium, $d\Omega$ is the angle of the scattered wave relative to the incident wave and $Q(r,\hat{s},t)$ is the source term [12].

Although conceptually straightforward, the RTT only provides an analytical solution in limiting cases. The most common limiting cases are the absorption-dominant limit and the scattering-dominant limit. However, in the NIR region of the optical spectrum, neither of such limiting cases apply. Therefore, although a powerful tool in the field of light transport in biological tissue, RTT falls short and thus a numerical approach is much more appropriate.

2.1.3. *Optical Properties of Biological Tissues.* The quantitative description of any biological tissue is given by its absorption and scattering coefficients, thickness, refractive index, and the anisotropy factor. The thickness of the tissue, in simple anatomical models, is defined as a constant without any spatial variations. This is highly inaccurate in regions of interest such as the adult head, where complex anatomical structure is key to accurate measurements and qualitative results. This optical property therefore provides value towards an experimental model only when the region of interest does not have any significant spatial variations. The refractive index in a homogeneous medium is assigned its usual meaning. However, in an inhomogeneous medium, the effective index of refraction is considered. Applying the relation of Waterman and Truell [34] for the case of uniformly distributed Rayleigh scatterers, the effective refractive index is

$$n_{eff} = n_m(1 + V\delta) \tag{6}$$

with n_m being the index of refraction of the medium, V being the volume fraction of scatterers in the medium and δ the fractional contrast between the indices of refraction present in the inhomogeneous medium. The anisotropy factor is a measure of the forward-directed scatter retained after the scattering event, and is given by

$$g = \frac{1}{4\pi W_0} \int_{4\pi} p(\hat{s} \cdot \hat{s}')(\hat{s} \cdot \hat{s}') d\Omega' = \frac{1}{2W_0} \int_{4\pi} p(\cos\theta) \cos\theta \sin\theta \, d\theta \tag{7}$$

where W_0 is the albedo given by $\mu_s/(\mu_s + \mu_a)$ and $\hat{s} \cdot \hat{s}' = \cos(\theta)$. The term is essentially the cosine-weighted average of the scattering. Lastly, the absorption and scattering coefficients retain the values assigned already. All the subcomponents present inside a tissue add to the total values of the optical properties for that specific tissue [12]. In the case of careful consideration, the optical properties of all the major subcomponents inside the tissue of interest are stated individually. In the case of an adequate approximation however, the optical properties of the subcomponents are embedded inside the tissue they are currently in; the tissue is uniformly defined by the said optical properties. This project follows the latter approximation due to its computational efficiency.

Scientific literature reports a large variability of reported optical properties for biological tissues. This raises the need to obtain those that are accurate for each application [15]. An important consideration that assists in the correct identification of the optical properties is the theoretical

calculation of such, through their biochemical composition and the interaction of light therein. The utilised mathematical models involve both the calculation of the baseline absorption and scattering of the tissue and then the calculation of the optical properties of the major absorbers and scatterers embedded inside that tissue. Haemoglobin and the average haemoglobin concentration, the arterio-venous oxygen saturation of haemoglobin in the blood, the average water content and average fat content are the major absorbers and hence the parameters that scale standard absorption spectra. Other minor absorbers present, such as melanin, bilirubin, and beta-carotene can also be added to the tissue absorption if their contribution is significant [14]. Cellular and subcellular organelles are the major scatterers in tissue. The organelles themselves act as Mie scatterers while the organelle and cellular membranes act as Rayleigh scatterers [12]. When using experimental procedures, there is a notable observation about the variability of the optical properties arising from the handling and preparation methods of a tissue sample [14]. It is logical that other factors such as age and health of the individual that the tissue sample was extracted affect the optical properties, but it is also rather imperative to consider that handling and preparation of the sample is critical to the values obtained. It can be inferred from scientific literature that, in the hypothetical scenario that five identical tissue samples are obtained from the same patient for experimental purposes, the measured optical properties will differ if different handling and preparation procedures are used. The optical properties also exhibit differences depending on whether the study is done in vivo or in vitro; clearly in vivo is preferable but not always the de facto approach. In vitro excised tissue samples undergo structural alterations, blood drainage, and temperature changes [17]. The significance of the handling and preparation methods as well as the in vivo – in vitro studies and their effect on the acquired optical properties on skin tissue samples are brilliantly addressed by Mignon et al. [15]. Contextualisation of the complexity in the correct determination of an optical property is thoroughly analysed by Jacques [14]. Although conceptually straightforward, the mathematical models and equations necessary for an in-depth evaluation of the optical properties vary depending on the tissue's structural organisation [16].

Tissue optical properties affect both diagnostic and therapeutic applications of light. The ability of light to penetrate a tissue, interact with the tissue components and then leave the tissue for detection is key for diagnostics. The ability of light to deposit energy inside a tissue through the tissue's absorption properties is key to therapeutics. Hence, defining the optical properties of a tissue with high specificity is necessary for the proper fabrication of medical devices, for interpreting diagnostic measurements, and effective treatment planning [14]. NIRS, photodynamic therapy and laser-induced interstitial heating are all treatment techniques that require the optical properties of the head to be accurately defined for a successful treatment and dosimetry planning. Also, the heat-induced changes of the optical properties are an important consideration in such treatments, and they should be quantified as well [18]. Accurate identification of optical properties provides information of medical significance on the structure of the tissue and the chromophore content, which offer insight on the distinction between normal and pathological tissue.

2.2. Monte Carlo Simulations

In practical situations where one wishes to quantify the light transport process inside a given tissue, considerations regarding complex geometries, spatial variations, and a variety of light sources are involved. The RTT cannot provide an analytical solution for most of these situations, and for those of which it is possible, it proves to be a greatly complicated process. A numerical approach is therefore the practical solution. Monte Carlo methods have been characterized as the "gold standard" method for simulating light transport in biological tissue, since they can solve the RTE with any desired accuracy. They carry however, a large computational load, and since they are statistical in nature, a large number of photons should be simulated [19].

2.2.1. *Simulating light transport in biological tissues.* The most realistic and intuitive scenario of photon propagation is through a multi-layered tissue [21]. Each layer is described by the absorption (μ_a) and scattering (μ_s) coefficients, the thickness, refractive index (n) and anisotropy factor (g). To account for

multiple scattering and record all the physical quantities of interest, all while tracking the propagation of the photon inside the tissue model, three different coordinate systems are used. The first, cartesian coordinate system, with its z-axis perpendicular to the tissue model, traces the photon movement. The second, cylindrical coordinate, with its z-axis aligned with that of the cartesian system, records internal photon absorption as function of r and z. It also scores the diffuse reflectance and diffuse transmittance as a function of θ and z. The third, moving spherical coordinate system, with its z-axis dynamically aligned with the direction of photon propagation is used to sample the change in the direction of the propagation. The photon direction is then updated from the cartesian system. A 2D homogeneous grid system in the r (cylindrical) and z (cartesian-cylindrical) directions is used to score photon absorption. Similarly, a 2D homogeneous grid system in the r and α directions of the cylindrical system is used to score diffuse reflectance and transmittance. The four physical quantities recorded are then, the total reflectance and transmittance, and the total photon absorption; the fluence distribution, is calculated using the recorded photon deposition. Total reflectance and transmittance are given as a summation of the diffuse and that which occurs on the air-matter boundary. The values of each of the physical quantities are estimated by the average of multiple independent samples (photon packet propagation). Monte Carlo, therefore, estimates ensemble-averaged quantities [20,21].

The simulation of the photon propagation is modelled as a persistent random walk. The location is defined by the cartesian coordinates and the direction of travel by the directional cosines (τ_x, τ_y, τ_z). The photon packet is given an initial weight W, equal to 1, and as it traverses through the tissue model, the assigned probabilities for absorption, scatter, reflection, and transmission at each interaction site lower the value of that weight until it reaches zero. The step sizes are incremented until such an interaction site is reached. At the interaction site, the absorption and scattering probabilities are calculated, and as mentioned, the weight decreases. Multiple interaction sites are encountered and, at a given boundary, reflection and transmission probabilities are also calculated. All the relevant variables in the system that represent the photon are updated as well as the parameters corresponding to physical quantities. The photon packet can be terminated naturally once its energy (weight W) is depleted inside the tissue due to the interactions, or when it is either reflected or transmitted out of the tissue model [20,21].

Cerebral haemodynamics in the adult head are therefore quantified and analysed using Monte Carlo methods. The complex geometries, and especially the irregular boundaries and undulating layers found in brain tissue, have no analytical solutions, but cannot be simulated using simple slab layers either. With mesh models being an ever-increasing integrative feature necessary for neuroimaging modalities and clinical imaging examinations, including functional NIRS, Electroencephalography (EEG), transcranial direct current stimulation (tCDS) and transcranial magnetic stimulation (TMS), this project hence utilised tetrahedral mesh models created using the Brain2Mesh open-source meshing software [22,23,24]. Light transport inside the mesh model was simulated using the MCX algorithm, as illustrated in figure 1.

2.3. The adult head

Improvements in the fields of biomedicine and medical physics have fabricated medical technologies that revolutionised the diagnosis, monitoring and treatment of brain-related diseases and neurological disorders directly affecting the brain. The anatomy of the adult head is undoubtedly complex; due to the high functioning abilities of the constituent tissues, each of those tissues is split into other, more singly defined regions. As an example, some common regions of the brain that are each responsible for specific cognitive behaviours or sensorimotor tasks include the frontal, parietal, and occipital lobes. Similarly, there are 22 different bones that are present in the head that are commonly referred to as the 'skull.' Absorbers and scatterers are present in each region of those tissues and hence contribute to the optical properties of that specific region of the tissue.

Biomedical optics is currently a promising candidate for the fabrication of new innovative technologies, however, the requirements for specificity of the optical properties of each region of the tissue poses constraints that need to be addressed.
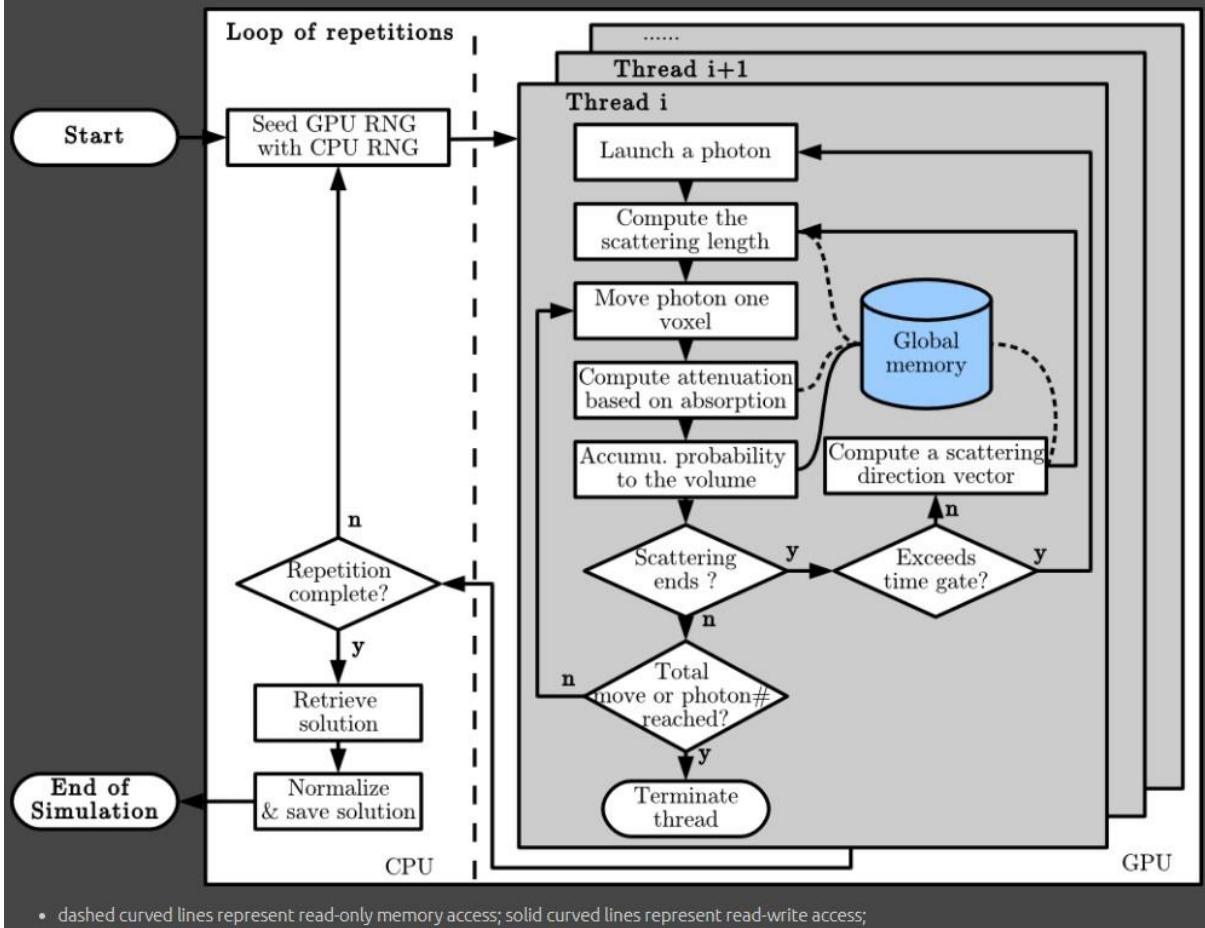
Figure 1: The algorithm used by MCX for the simulation of light transport inside a model of biological tissue. Reprinted from [25] with permission from the developer of the website.

3. Methodology

A head atlas from the John E. Richards Lab Neurodevelopmental MRI Database was converted to a five-layered tetrahedral mesh-based model in MATLAB using the open-source software Brain2Mesh [9,10]. The optical properties of those five layers, namely the scalp, cranial bone, cerebrospinal fluid (CSF), grey matter (GM) and white matter (WM) were obtained by consulting relevant literature. Due to the high variability of the optical properties present in the current literature, the acquisition of said properties were from consulted papers which had considered mathematical theories based on the biochemical composition of the tissue(s) or experimentation techniques where the handling and preparation of the tissue(s) had retained their biochemical composition with only very minor alterations. The acquired values for all five layers are listed in Table 1.

Simulations were carried out in MMCLAB [25] using a Lenovo Series 3 laptop, with Intel® Core™ i5-10300H processor, 8GB RAM and an Nvidia GeForce GTX-1650 4GB graphics processing unit. MMCLAB is an open-source software that is part of the MCXStudio package. The package also includes a user interface for Monte Carlo light transport simulations through slab-layered models constructed with simple geometric shapes. Although a solid knowledge of MATLAB and a greater length of time is required to create the mesh model using MMCLAB, it is highly more accurate, with fluence precision results that largely outweigh the capabilities of any slab-layered model constructed out of simple shapes, or any voxelated volume. Mesh models in general draw large advantage over voxelated volumes and

layered slabs, especially in the simulation of a complex anatomy such as the adult head. Further information on the advantages in the use of a mesh model over the other two modelling methodologies are given in Tran et al [23]. In addition, modelling brain anatomy accurately also plays important roles in other quantitative neuroimaging modalities, such as electro- and magnetoencephalography [23].

Wavelength	650 nm	700 nm	800 nm	900 nm	1000 nm	1100 nm
μ_a (mm^{-1})	0.039	0.024	0.025	0.035	0.048	0.042
μ_s (mm^{-1})	35.487	31.130	29.286	26.017	28.32	27.08
g	0.924	0.931	0.937	0.941	0..90	0.90
n	1.40	1.40	1.40	1.40	1.40	1.40
SCALP						
μ_a (mm^{-1})	0.039	0.024	0.025	0.035	0.048	0.042
μ_s (mm^{-1})	35.487	31.130	29.286	26.017	28.32	27.08
g	0.924	0.931	0.937	0.941	0..90	0.90
n	1.43	1.43	1.43	1.43	1.43	1.43
CRANIAL BONE						
μ_a (mm^{-1})	0.004	0.004	0.004	0.004	0.004	0.004
μ_s (mm^{-1})	2.40	2.40	2.40	2.40	2.40	2.40
g	0.89	0.89	0.89	0.89	0.89	0.89
n	1.33	1.33	1.33	1.33	1.33	1.33
CEREBROSPINAL FLUID						
μ_a (mm^{-1})	0.017	0.02	0.02	0.03	0.06	0.05
μ_s (mm^{-1})	9.01	8.41	7.70	6.73	6.16	5.51
g	0.89	0.90	0.90	0.90	0.90	0.90
n	1.37	1.37	1.37	1.37	1.37	1.37
GREY MATTER						
μ_a (mm^{-1})	0.08	0.08	0.08	0.10	0.12	0.10
μ_s (mm^{-1})	40.82	39.31	36.45	32.95	30.54	28.32
g	0.86	0.85	0.87	0.88	0.88	0.88
n	1.37	1.37	1.37	1.37	1.37	1.37
WHITE MATTER						

Table 1; The optical properties for the five layers of the adult head model acquired from papers with accurate measurements. Values were collected from [12,30,31,32].

The tetrahedral mesh was incorporated into the MMCLAB program, with each layer defined by the four optical properties and their corresponding values as listed in Table 1. Eight pencil-beam sources were inserted onto the outer layer of the scalp, with each emitting 10 million photons inside the head at a 10ns time-resolved pulse. Fluence distribution and the detected photon information are saved as the output of the simulation. Post-simulation data processing converts the single-pulse data to continuous-wave (CW) as it is more applicable for the current situation of measurements in this model. This is since the behaviour of light inside the tissue is best described using the mathematical approaches and tissue approximations that are conveyed within the theory of CW light. It is important to mention, that at the time of writing, MMCLAB does not support multiple sources, however, a loop can be used to define multiple sources, with their fluence distributions summed and then averaged over the corresponding number of sources.

Cerebral haemodynamics are affected by the oxygenation of haemoglobin. Absorption and scattering coefficients of the cerebral tissue are altered depending on the oxygen saturation of the blood-carrying protein. This is due to the fact, that haemoglobin is a major contributor to the absorption properties of the cerebral tissue. Mathematical relationships obtained from literature, quantitively measure the change in the absorption coefficient and hence the scattering coefficient caused by the decreasing oxygenation

levels. For all other tissues, their optical properties remain unaffected, as there is no blood entering those tissues. Also, the anisotropy factors and refractive indices of the cerebral tissues are not altered either. The change in the absorption and scattering coefficients of the brain are quantified using the equations from [26,27]:

$$\mu_{a,\lambda} = \varepsilon_{HbO_2,\lambda}[HbO_2] + \varepsilon_{Hb,\lambda}[Hb] + B(\lambda) \qquad (8)$$

$$\mu_s' = \frac{S_{AC}^2 - S_\Phi^2}{3\mu_a} - \mu_a \qquad (9)$$

Equation (9) includes the reduced scattering coefficient, which relates to μ_s through $\mu_s' = \mu_s(1 - g)$. The ε_{HbO_2} and ε_{Hb} are the extinction coefficients for the oxyhaemoglobin and deoxyhaemoglobin, respectively. The $B(\lambda)$ term is the value of 0.7x the absorption coefficient of water. The S_{AC} and S_Φ are the slopes of the graphs 6b and 6c of [28]. These were measured to be $S_{AC} = 0.7346mm^{-1}$ and $S_\Phi = 0.07280mm^{-1}$. The absorption coefficient of water and the extinction coefficients for the oxyhaemoglobin and deoxyhaemoglobin were measured for the six wavelengths of interest as given in table 1, using the graphs from [14,29] by means of plot digitising.

The oxygen saturation and haemoglobin are related through [26]:

$$HbT = HbO_2 + Hb \qquad (10)$$

$$StO_2 = \frac{HbO_2}{HbT} \qquad (11)$$

HbO_2 and Hb are the oxyhaemoglobin and deoxyhaemoglobin respectively, with HbT being the total haemoglobin summing up to unity. The values of oxygen saturation from 50% to 100% and their corresponding absorption and scattering coefficients were calculated for 650 nm, 700 nm, 900 nm and 1100 nm using the equations given above. The 700 nm and 800 nm wavelengths were selectively excluded from further usage because the change in their absorption and scattering coefficients was minimal without any notable changes. Figure 2 depicts the change in μ_a and μ_s for those wavelengths of interest with oxygen saturation levels.
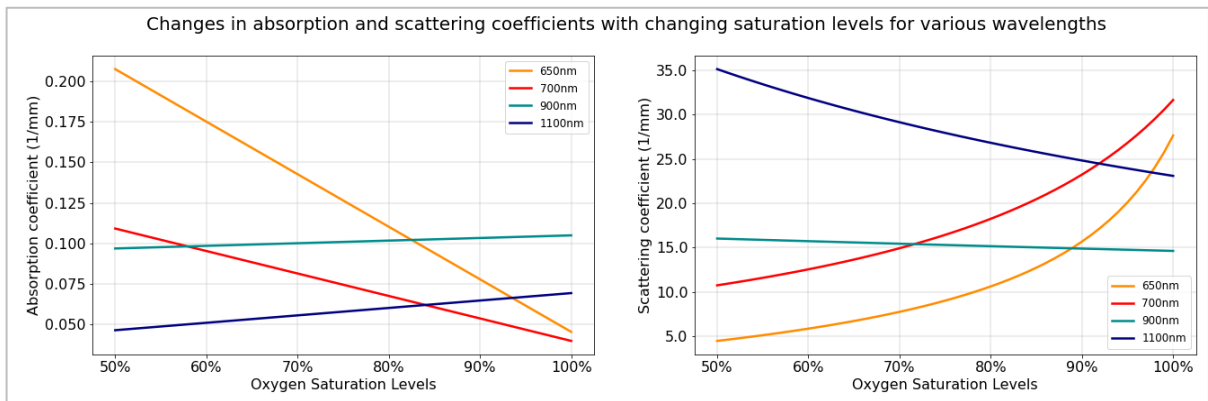

Figure 2: The change in absorption and scattering coefficients as a function of the oxygen saturation in the cerebral tissue. Four wavelengths of interest are included.

The above equations calculate the desired optical properties for the brain without any distinctions between the different regions. Therefore, the calculated values for both the grey matter and white matter will be identical during the simulations for the quantification of the oxygen saturation effect on the haemodynamic response. In total, four saturation levels were considered at 98%, 90%, 60% and 50%

for the four wavelengths of interest. Therefore, the new values for μ_a and μ_s of the brain are given in table 2.

Oxygen Saturation	Wavelength (nm)			
	650	700	900	1100
98%	0.052 / 24.058	0.042 / 29.509	0.105 / 14.679	0.068 / 23.404
90%	0.078 / 15.677	0.054 / 23.224	0.103 / 14.890	0.065 / 24.810
60%	0.175 / 5.871	0.095 / 12.552	0.098 / 15.725	0.051 / 31.844
50%	0.208 / 4.491	0.109 / 10.753	0.097 / 16.020	0.046 / 35.102

Table 2: The values for the absorption and scattering coefficients at the four wavelengths of interest and four oxygen saturation levels. Both coefficients are included on the same cell for each λ-StO₂ combination as μ_a / μ_s.

4. Results

The visualisation of the fluence distribution at a given wavelength was carried out in coronal planes instead of the whole head. In each of the coronal planes considered, eight sources were introduced at locations on the scalp with beam directions that assisted for maximal depth penetration. The choice of fluence representation in this manner provides a more informative illustration of the change in fluence with decreasing cerebral oxygenation, rather than a 3D view. Figure 3 shows the fluence distribution of four simulation scenarios at the 800 nm wavelength for different coronal planes, using the optical properties from table 1. This was done to ensure that the fluence is well-quantified for different coronal planes using the same number of sources and photons at the same wavelength. In all simulations, the fluence is represented in log scale and only the upper half of the head is modelled to constraint the area of interest for clearer deductions.
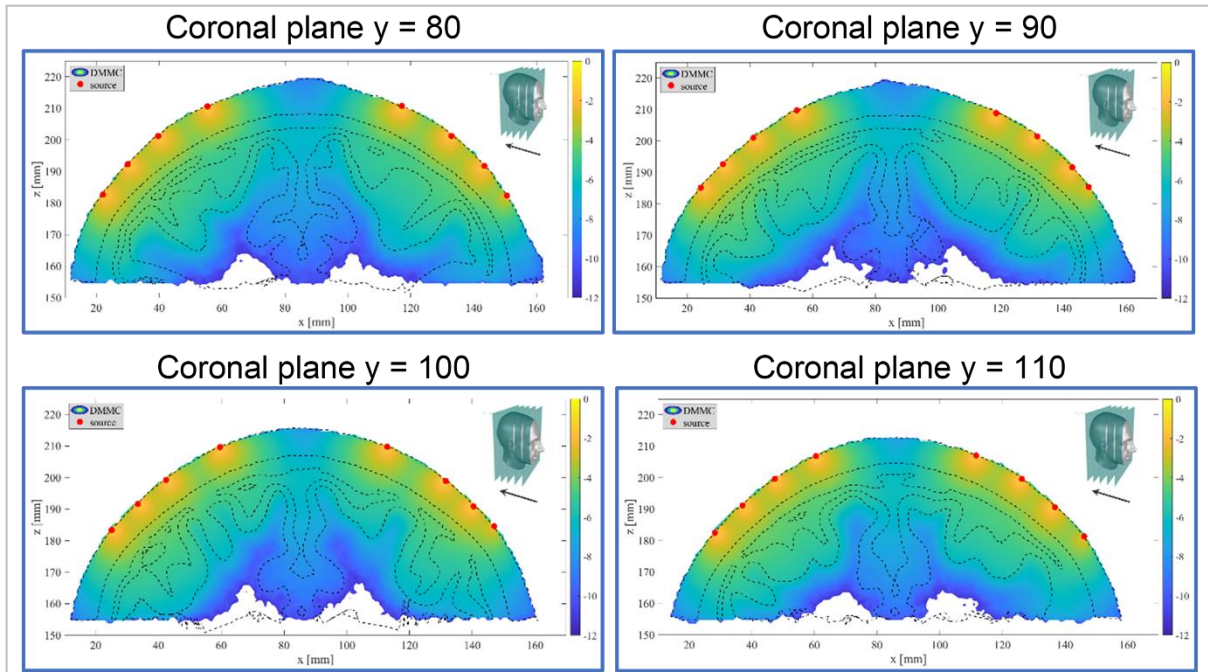

Figure 3: The fluence distribution for the 800 nm wavelength at different coronal planes using 8 sources and 80 million photons. In all coronal planes, for all wavelengths, the distribution is quantified properly and accurately. Four such graphs are included in this article for the y = 80, 90, 100 and 110mm coronal planes of the head model. Coronal plane image on the top right of each graph was reprinted from [24] with permission [Elsevier].

Therefore, the applicability of the method for fluence distribution representation is applicable in the case of decreasing oxygen saturation levels to be observed at any coronal plane. The fluence was therefore measured for the four wavelengths of interest, each at the four oxygen saturation levels previously determined, replacing the absorption and scattering coefficients for the white and grey matter of table 1 with those from table 2. The results of the 16 simulations are presented in figure 4 as a 4x4 matrix; log scale is maintained for the fluence as in figure 3.
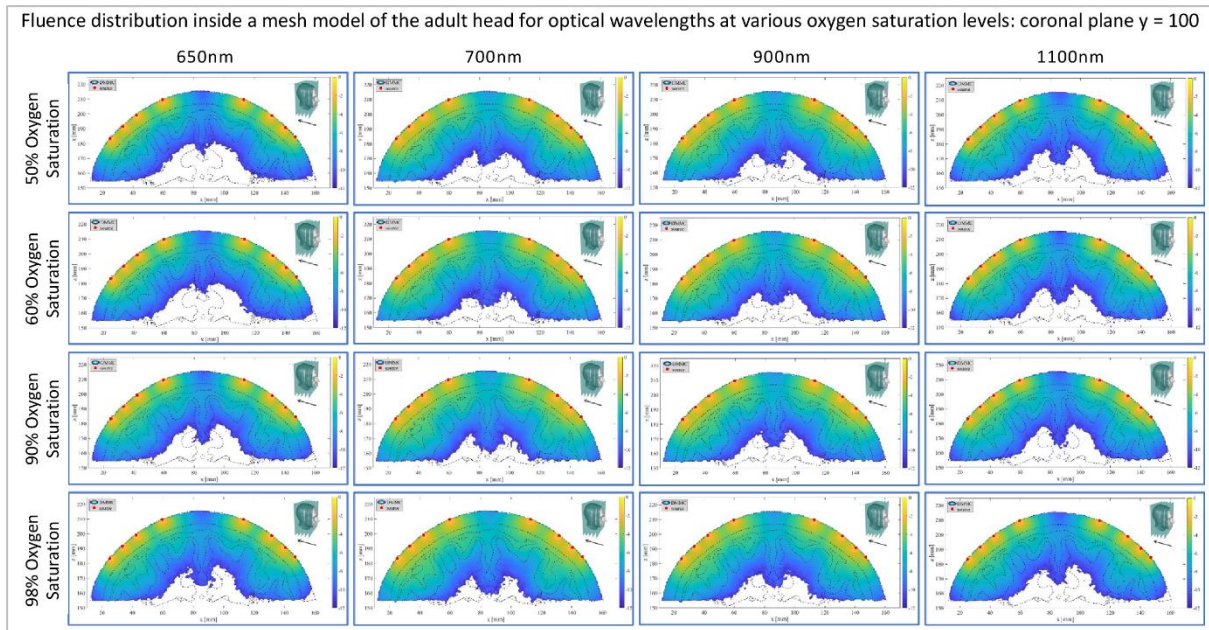

Figure 4: The decrease in fluence is clearly observed in the 650 nm wavelength, as the blue region steadily decreases with decreasing cerebral oxygenation. Light reaches deeper into the tissue when oxygenation is at healthy levels (≥90%). Similarly, the fluence in the 700 nm wavelength is still noticeable, as the blue region decreases at the undhealthy oxygen saturation levels, however, the difference is only clearly quantified at large oxygen depletion levels. The fluence for the 900 nm and 1100 nm wavelengths does not produce any concluding evidence for noticeable differences.

The 98% oxygenation level at the 900 nm and 650 nm were then subtracted from each other; similarly for the 50% oxygentation case. Dual-wavelength pulse oximeters use this technique in order to define the oxy-deoxy haemoglobin concentration in a patient [27]. Following a similar approach, the fluence difference was obtained for the 900 nm – 650 nm dual-wavelength. However, as figure 5 shows, there is not any significant difference observed in the fluence for neither of the 50% nor 98% oxygen saturation.
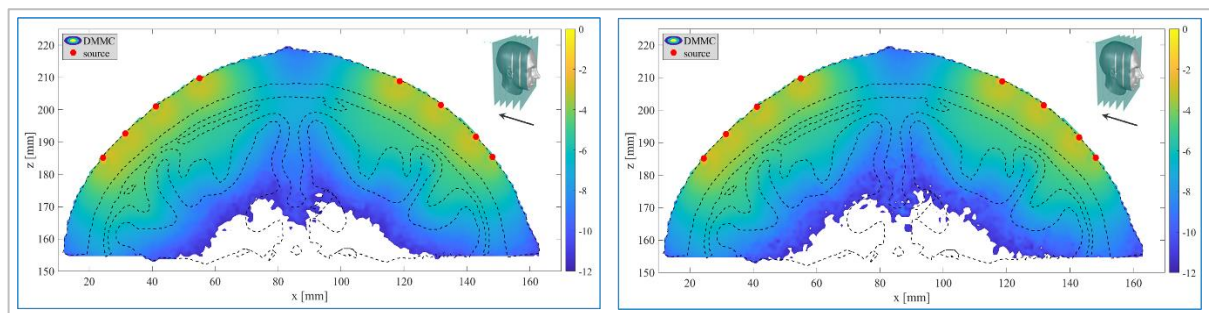

Figure 5: The fluence difference for the 50% (left) and 98% (right) oxygenation levels for the dual-wavelength 900nm-650nm. There is no significant difference observed in the two flunce distributions compared to those in figure 4.

5. Discussion and Future Work

Quantification of cerebral haemodynamics has been successfully illustrated for the 650 nm and 700 nm wavelengths, but without any particularly informative results for the 900 nm and 1100 nm cases. In consideration however, of the computational limitations on the number of photons simulated in each run (~80 million), more informative results can be acquired with the use of billions of photons. Using such a number of photons implies that the fluence distribution will be sufficiently larger so as to quantify even the slightest fractional differences. In a clinical scenario, the use of photons in the magnitude of billions and their detection is a matter of standard procedure. Currently, at the level of computational limitations, the energy deposition of the simulated photons is represented in a scale of log_{10}. Therefore, the blue regions on the graphs correspond to a fluence value of 10^{-10} to 10^{-11}, an almost negligible value that clinical detectors are not sensitive enough to measure. In a simulation-based approach, the weight of the photon can be detected even at negligible values - the scale could just as easily have a minimum value of e.g., 10^{-30} represented in log scale. In a real-world clinical scenario however, the detectable penetration and quantification of light through the head is extremely unlikely at negligible values, yet for accurate detection as well. An increase, therefore, in the number of photons to billions will both allow for the accurate detection and quantification of light transport inside the head, and for the detection of fractional differences in the fluence for the correct identification of the cerebral oxygenation levels. Accordingly, the dual-wavelength 900 nm - 650 nm fluence difference will also be more appropriately quantified, with the difference being visible for small fractional changes in the region of the brain. As is the nature of this study, we find insights at single wavelength tests but clinical results require an investigation in multiple wavelengths as the difference of interaction of the biological layers could offer actionable information. This is clearly seen in the case of pulse oximeters that use red and NIR wavelength sources.

The current model used for the simulations includes five layers. The optical properties of those layers are taken to be the weighted average of all the subcomponents acting as the major absorbers and scatterers within the given tissues. The Brain2Mesh software, however, is highly adjustable and models can be created with higher numbers of layers as well. A tetrahedral mesh model of the adult head can be constructed to include individual brain regions and, extending to further meticulous simulations, the introduction of the subcomponents of each layer can be inserted into the model as well. In that regard, the accuracy of the model increases when considering the introduction of the subcomponents in a uniform distribution-based manner with their equivalent optical properties. It is important to state that the subcomponents' positions inside a tissue are difficult to pinpoint with high detail in the micrometre scale, therefore a uniform distribution-based approach is highly favourable for such a situation. Increasing the accuracy of the model also provides a fluence that increases in specificity, at the expense of larger computing power and longer time frames for the simulations to take place.

An improved model of that manner, and through the use of billions of photons, the results can provide valuable insight on the healthy and unhealthy brain functioning at specific regions of the brain instead of just the whole brain. Therefore, in a clinical diagnostics scenario, regions of the brain that are not oxygenated properly due to incurred damage or due to restrictive blood flow can be imaged using a technique that is comparatively affordable and has a high-resolution output. Ideally, these would be comparable to the current standard imaging modalities of MRI or CT. The inexpensive nature of the procedure and the fact that NIR light can be used constantly without any harm to the patient allows for the constant monitoring of the patient using an electrode setup connected to the scalp, with multiple sources sending light photons in the brain. A distinction should be made between the abnormal physiological response caused by congested blood flow or damage in a specific region of the brain. In both clinical situations, the current model detects the change in the optical properties of the brain and the improved model will detect the change in the optical properties of a specific brain region, specifically the absorption and scattering coefficients. The distinguishability of the two cases can be achieved by measuring the total energy deposited in for each region individually and then quantify the major contributors (absorbers and scatterers) of every region. Therefore, for the first case of congested blood flow in a brain region, one would observe that the blood in that region is less than the expected. This

also gives rise to the fact that, if the optical properties of a specific region are different than those expected, it could either be caused by the blood, or any other major contributor. Hence, by quantification of the energy deposition of all the major contributors, one can know exactly what biochemical component is not at the expected levels for healthy functioning. In the second case of damage to a specific brain region affecting the oxygen saturation levels, one can insightfully quantify the oxyhaemoglobin and deoxyhaemoglobin again with the same process: Deposited energy is measured, and a method such as the inverse adding doubling can be used to quantify the contributors and their present level at the specific region of interest [5]. The results however, for the biochemical composition of the region of interest will be different for the two cases.

Fluence distribution not only varies with changing optical properties, but it also varies with anatomy. Therefore, an atrophied brain caused by dementia will produce a much different fluence distribution than a healthy brain. However, for this model to be extended in those directions, it is required that emitted light should cover the whole head, by increasing the number of sources and the number of photons, which current experimental setup for Monte Carlo poses limitations due to computing power and GPU strength. Whole head simulation in this clinical scenario is important because brain atrophy has many stages in which anatomy changes gradually, therefore a whole head fluence distribution can accurately show which atrophy stage the brain is found [33].

The simulations were carried out in the NIR-I optical transparency window. Quantification of the cerebral haemodynamics through the change in oxygenation levels can also be made about using other optical transparency windows. Tissue optical properties are different than those in the NIR-I and might prove just as useful and be just as suitable light transport in the adult head as the NIR-I.

6. Conclusion
The experiment successfully achieved its objective of quantifying cerebral haemodynamics through light transport at decreasing oxygenation levels. Although a small number of photons were used due to computational limitations and GPU strength, the simulations for 650 nm and 700 nm wavelengths clearly illustrate the fluence reduction in the model as oxygen saturation decreases. The 900 nm and 1100 nm cases do not produce any noticeable difference, however, in the introduction of billions of photons, more informative results can be obtained. The optical properties used in the model were acquired from accurate scientific literature. Careful consideration should be given to the acquisition of such optical properties due to the high variability recorded in current literature. It is important to use optical properties that best reflect the tissues under examination as even a small difference in a given value can cause detectable changes in the fluence. The values that are chosen for any specific tissue should reflect the biochemical composition of that tissue, therefore, by correct evaluation of the biochemical composition, the accuracy of the optical properties can be defined. Therefore, literature papers that followed such procedures either through mathematical derivations or through experimental measurements were consulted for their optical properties. The equations for the absorption and scattering coefficients of the brain due to the change in oxy-deoxy haemoglobin were acquired from literature as well and inserted in the model. The potential extensions of the current model are also mentioned, along with the utility of translating such research into medical diagnostics modalities that can detect oxygen depletion in a given brain region or congested blood flow as well as brain atrophy. The experiment was carried out in the NIR-I optical transparency window, however, experimentation on the other optical transparency windows can also provide fruitful results.

References

[1] Golovynskyi, S., Golovynska, I., Stepanova, L., Datsenko, O., Liu, L., Qu, J. and Ohulchanskyy, T., 2018. Optical windows for head tissues in near-infrared and short-wave infrared regions: Approaching transcranial light applications. *Journal of Biophotonics*, [online] 11(12). Available at: <https://onlinelibrary.wiley.com/doi/abs/10.1002/jbio.201800141>.

[2] Leitgeb, R. and Baumann, B., 2018. Multimodal Optical Medical Imaging Concepts Based on Optical Coherence Tomography. *Frontiers in Physics*, [online] 6. Available at: <https://www.frontiersin.org/articles/10.3389/fphy.2018.00114/full>.

[3] Custo, A., Wells III, W., Barnett, A., Hillman, E. and Boas, D., 2006. Effective scattering coefficient of the cerebral spinal fluid in adult head models for diffuse optical imaging. *Applied Optics*, [online] 45(19), pp.4747-4755. Available at: <https://www.osapublishing.org/ao/abstract.cfm?uri=ao-45-19-4747>.

[4] Kallepalli, A. and B. James, D., 2020. Quantification and influence of skin chromophores for remote detection of anemic conditions. *Proceedings of SPIE*, [online] 11238. Available at: <https://www.spiedigitallibrary.org/conference-proceedings-of-spie/11238/2545784/Quantification-and-influence-of-skin-chromophores-for-remote-detection-of/10.1117/12.2545784.short>.

[5] Genina, E., Bashkatov, A. and Tuchin, V., 2008. Optical Clearing of Cranial Bone. *Advances in Optical Technologies*, [online] 2008. Available at: <https://www.hindawi.com/journals/aot/2008/267867/>.

[6] Sawosz, P., Wojtkiewicz, S., Kacprzak, M., Weigl, W., Borowska-Solonynko, A., Krajewski, P., Bejm, K., Milej, D., Ciszek, B., Maniewski, R. and Liebert, A., 2016. Human skull translucency: post mortem studies. *Biomedical Optics Express*, [online] 7(12), pp.5010-5020. Available at: <https://www.osapublishing.org/boe/fulltext.cfm?uri=boe-7-12-5010&id=354379>.

[7] Kurihara, K., Kawaguchi, H., Obata, T., Ito, H., Sakatani, K. and Okada, E., 2012. The influence of frontal sinus in brain activation measurements by near-infrared spectroscopy analyzed by realistic head models. *Biomedical Optics Express*, [online] 3(9), pp.2121-2130. Available at: <https://www.osapublishing.org/boe/fulltext.cfm?uri=boe-3-9-2121&id=240608>.

[8] Draghici, A., Potart, D., Hollmann, J., Pera, V., Fang, Q., DiMarzio, C., Andrew Taylor, J., Niedre, M. and Shefelbine, S., 2017. Near infrared spectroscopy for measuring changes in bone hemoglobin content after exercise in individuals with spinal cord injury. *Journal of Orthopaedic Research*, [online] 36(1), pp.183-191. Available at: <https://onlinelibrary.wiley.com/doi/abs/10.1002/jor.23622>.

[9] John E. Richards Lab. n.d. *Neurodevelopmental MRI Database*. [online] Available at: <https://jerlab.sc.edu/projects/neurodevelopmental-mri-database/> [Accessed 29 March 2021].

[10] Fang, Q., n.d. *Brain2Mesh - A one-liner brain mesh generator*. [online] Mcx.space. Available at: <http://mcx.space/brain2mesh/> [Accessed 29 March 2021].

[11] Secomb, T., 2016. Hemodynamics. *Comprehensive Physiology*, [online] 6(2), pp.975-1003. Available at: <https://onlinelibrary.wiley.com/doi/abs/10.1002/cphy.c150038>.

[12] Vo-Dinh, T., 2003. *Biomedical photonics handbook*. 1st ed. CRC Press.

[13] Hoffman, C. and Driggers, R., 2015. *Encyclopedia of optical and photonic engineering*. 2nd ed. CRC Press, Ch. 72.

[14] Jacques, S., 2013. Optical properties of biological tissues: a review. *Physics in Medicine and Biology*, [online] 58(14). Available at: <https://iopscience.iop.org/article/10.1088/0031-9155/58/14/5007>.

[15] Mignon, C., Tobin, D., Zeitouny, M. and Uzunbajakava, N., 2018. Shedding light on the variability of optical skin properties: finding a path towards more accurate prediction of light propagation in human cutaneous compartments. *Biomedical Optics Express*, [online] 9(2), pp.852-872. Available at: <https://doi.org/10.1364/BOE.9.000852>.

[16] Tuchin, V., 1997. Light scattering study of tissues. *Physics-Uspekhi*, [online] 40(5), pp.495-515. Available at: <https://iopscience.iop.org/article/10.1070/PU1997v040n05ABEH000236>.

[17] Bevilacqua, F., Piguet, D., Marquet, P., Gross, J., Tromberg, B. and Depeursinge, C., 1999. In vivo local determination of tissue optical properties: applications to human brain. *Applied Optics*, [online] 38(22), pp.4939-4950. Available at: <https://doi.org/10.1364/AO.38.004939>.

[18] Yaroslavsky, A., Schulze, P., Yaroslavsky, I., Schober, R., Ulrich, F. and Schwarzmaier, H., 2002.

Optical properties of selected native and coagulated human brain tissues in vitro in the visible and near infrared spectral range. *Physics in Medicine and Biology*, [online] 47(12), pp.2059-2073. Available at: <https://iopscience.iop.org/article/10.1088/0031-9155/47/12/305>.

[19]   Zhu, C. and Liu, Q., 2013. Review of Monte Carlo modeling of light transport in tissues. *Journal of Biomedical Optics*, [online] 18(5). Available at: <https://doi.org/10.1117/1.JBO.18.5.050902>.

[20]   Wang, L. and Wu, H., 2007. *Biomedical optics*. 1st ed. Hoboken, N.J.: Wiley-Interscience, pp.37-65.

[21]   Wang, L., Jacques, S. and Zheng, L., 1995. MCML—Monte Carlo modeling of light transport in multi-layered tissues. *Computer Methods and Programs in Biomedicine*, [online] 47(2), pp.131-146. Available at: <https://www.sciencedirect.com/science/article/pii/016926079501640F?via%3Dihub>.

[22]   Tran, A. and Fang, Q., 2017. Fast and high-quality tetrahedral mesh generation from neuroanatomical scans.

[23]   Tran, A., Yan, S. and Fang, Q., 2020. Improving model-based functional near-infrared spectroscopy analysis using mesh-based anatomical and light-transport models. *Neurophotonics*, [online] 7(1). Available at: <https://doi.org/10.1117/1.NPh.7.1.015008>.

[24]   Skals, S., Ellena, T., Subic, A., Mustafa, H. and Pang, T., 2016. Improving fit of bicycle helmet liners using 3D anthropometric data. *International Journal of Industrial Ergonomics, [online] 55, pp.86-95. Available at: <https://doi.org/10.1016/j.ergon.2016.08.009>.*

[25]   Fang, Q., Yan, S., Yuan, Y., Nina-Paracevino, F., Yu, L., Yao, R., Kaeli, D., Intes, X. and Arridge, S., n.d. Monte Carlo eXtreme - The Photon Player. [online] Mcx.space. Available at: <http://mcx.space/> [Accessed 12 April 2021].

[26]   Barker, J., Panigrahy, A. and Huppert, T., 2014. Accuracy of oxygen saturation and total hemoglobin estimates in the neonatal brain using the semi-infinite slab model for FD-NIRS data analysis. *Biomedical Optics Express*, 5(12), pp.4300-4312.

[27]   McIntosh, M., Shahani, U., Boulton, R. and McCulloch, D., 2010. Absolute Quantification of Oxygenated Hemoglobin within the Visual Cortex with Functional Near Infrared Spectroscopy (fNIRS). *Investigative Opthalmology & Visual Science*, [online] 51(9), pp.4856-4860. Available at: <https://doi.org/10.1167/iovs.09-4940>.

[28]   Fantini, S., Franceschini, M. and Gratton, E., 1994. Semi-infinite-geometry boundary problem for light migration in highly scattering media: a frequency-domain study in the diffusion approximation. *Journal of the Optical Society of America B*, [online] 11(10), pp.2128-2138. Available at: <https://doi.org/10.1364/JOSAB.11.002128>.

[29]   Kim, J., Xia, M. and Liu, H., 2005. Extinction coefficients of hemoglobin for near-infrared spectroscopy of tissue. *IEEE Engineering in Medicine and Biology Magazine*, [online] 24(2), pp.118-121. Available at: <https://ieeexplore.ieee.org/document/1411359>.

[30]   Wu, L., Lin, Y. and Li, T., 2017. Effect of Human Brain Edema on Light Propagation: A Monte Carlo Modeling Based on the Visible Chinese Human Dataset. *IEEE Photonics Journal*, 9(5), pp.1-10.

[31]   Genina, E., Bashkatov, A. and Tuchin, V., 2008. Optical Clearing of Cranial Bone. *Advances in Optical Technologies*, [online] 2008, pp.1-8. Available at: <https://www.hindawi.com/journals/aot/2008/267867/>.

[32]   Firbank, M., Hiraoka, M., Essenpreis, M. and Delpy, D., 1993. Measurement of the optical properties of the skull in the wavelength range 650-950 nm. *Physics in Medicine and Biology*, [online] 38(4), pp.503-510. Available at: <https://iopscience.iop.org/article/10.1088/0031-9155/38/4/002>.

[33]   Ancora, D., Qiu, L., Zacharakis, G., Spinelli, L., Torricelli, A. and Pifferi, A., 2018. Noninvasive optical estimation of CSF thickness for brain-atrophy monitoring. *Biomedical Optics Express*, [online] 9(9), pp.4094-4112. Available at: <https://doi.org/10.1364/BOE.9.004094>.

[34]   Waterman, P. and Truell, R., 2004. Multiple Scattering of Waves. *Journal of Mathematical Physics*, [online] 2(4), pp.512-537. Available at: <https://doi.org/10.1063/1.1703737>.